



UNIVERSITÀ DEGLI STUDI DI PADOVA

Dipartimento di Fisica e Astronomia “Galileo Galilei”

Corso di Laurea in Fisica

Tesi di Laurea

Infrared and Raman spectra from first-principles calculations for the MAPbI_3 perovskite and derived materials

Relatore

Prof. Paolo Umari

Laureanda

Giulia Campesan

Anno Accademico 2019/2020

Abstract

Infrared and Raman spectroscopies are often applied in materials characterization.

In order to obtain an optimal identification of the aforementioned spectra particularities, the comparison with accurate theoretical simulations, based on first-principles methods, such as density-functional theory (DFT), can be helpful.

The objective of the present thesis is the calculation of the infrared (IR) and Raman spectra for the MAPbI_3 perovskite and derived materials.

These materials have recently aroused interest due to their potential applications in photovoltaic cells. The IR and Raman spectra have been computed starting from vibrational modes and dielectric tensors that have been originally obtained using the DFT code Quantum-Espresso.

The calculated spectra have then been compared to their experimental counterparts.

Contents

1	Infrared and Raman spectra	7
1.1	Infrared spectrum: dielectric complex function $\epsilon(\omega)$	7
1.2	Raman spectrum: reduced cross-section	8
2	Application to vitreous Silica ($v\text{-SiO}_2$)	11
3	Application to methylammonium lead triiodide perovskite: $\text{CH}_3\text{NH}_3\text{PbI}_3$	15
3.1	Comparison of measured and computed Raman spectra	20
3.2	Inorganic network contribution	21
	Conclusion	23
	Bibliography	25

Chapter 1

Infrared and Raman spectra

In this chapter, we recall the main theoretical concepts underlying Raman and infrared spectroscopies and we explain how we have exploited them to calculate the spectra that will be discussed in the next sections.

The physical picture we are considering is the process of light impinging upon materials, that can turn out in absorption, elastic or inelastic scattering.

In particular, in the case of a wavelength longer than the ones inducing electronic excitations, the interaction involves vibrational modes, due to energy exchange between incident light photons and lattice phonons.

In the case of one-photon absorption, considering radiation in the infrared region, a phonon will be created through dielectric coupling with the oscillating electric field, when it can induce a change in the system dipole moment.

Instead, in the case of scattering, we have two possible scenarios: either the photon energy is conserved, through the elastic Rayleigh scattering, or it is not: this is the aforementioned Raman scattering.

Focusing on Raman diffusion, during molecule-light interaction, a phonon can be created, in the so-called Stokes process, meaning that outgoing light frequency ν_{out} will be lower than the one of incoming laser light ν_{in} , by the frequency ν of the created phonon: $\nu_{out} = \nu_{in} - \nu$, or the phonon can be destroyed, in the symmetric anti-Stokes process. Moreover, a transition will be Raman active if the involved phonon can modify the molecular polarizability.

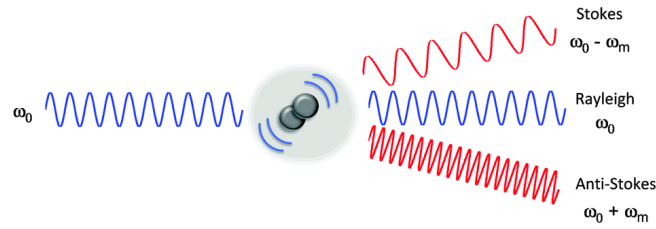


Figure 1.1: visual representation (from [6]) of elastic Rayleigh scattering and inelastic Stokes and anti-Stokes Raman processes.

1.1 Infrared spectrum: dielectric complex function $\epsilon(\omega)$

We analyze the dielectric properties of the studied materials through the computation from first-principles of the complex dielectric function $\epsilon(\omega)$, that in the low-frequency range can be written as:

$$\epsilon(\omega) = 1 + \sum_{n=1, N_{ph}} \left(\frac{F_n^2}{\omega_n^2 - (\omega + i\eta)^2} \right) + \frac{F_{el}^2}{\omega_{el}^2 - (\omega + i\eta_{el})^2}, \quad (1.1)$$

where N_{ph} is the number of phonon modes at the center zone Γ , that for a material which presents N atoms in the unit cell of volume Ω are equal to $3N$. The 3 lowest frequency modes correspond to translations and will be ignored further on since they don't correspond to an increase in internal energy. Then

$$F_n = \left(\sum_{i=1,3} \left(\sum_{I=1,N,j=1,3} \frac{4\pi}{3\Omega} \frac{Z_{I,ij}^* v_{I,j}^n}{\sqrt{M_I}} \right)^2 \right)^{\frac{1}{2}}$$

are the oscillator strengths, ω_{el} is the electronic band gap, η , η_{el} are proper broadening factors and i, j are the Cartesian components indexes. ω_n and \mathbf{v}^n are the phonon frequencies and normal modes found respectively as eigenvalues and orthonormal eigenvectors of the analytical part of the dynamical matrix:

$$D_{Ii,Jj} = \frac{1}{\sqrt{M_I M_J}} \frac{\partial^2 E_{tot}}{\partial r_{Ii} \partial r_{Jj}},$$

where E_{tot} is the total energy of the system, M_I is the mass of the I_{th} atom and r_{Ii} is the i_{th} component of its Cartesian position. In particular, from the normalized eigenmodes \mathbf{v}^n we define the atomic displacements $u_{I,j}^n = \frac{v_{I,j}^n}{\sqrt{M_I}}$ related to mode n , the I_{th} atom and the j_{th} component.

The eigenvalues and eigenvectors we have been furnished with to compute our spectra have been precendently obtained using first-principles calculations, relying on the density-functional perturbation theory (DFPT) approach. We were then able to calculate the atomic forces \mathbf{F}_I upon the application of a finite electric field to our system. Considering finite differences of \mathbf{F}_I over the electric field, the Born effective charge tensors $Z_{I,ij}^* = -\frac{\partial F_{Ij}}{\partial E_i} = -\frac{\Delta F_{Ij}}{\Delta E_i}$

can be computed.

In particular, we are interested in the real and imaginary parts of the dielectric function, respectively $\epsilon_1(\omega)$ and $\epsilon_2(\omega)$ [7]:

$$\epsilon_1(\omega) = \epsilon^\infty + \sum_n \frac{|F_n|^2}{\omega^2 - \omega_n^2}, \quad (1.2)$$

$$\epsilon_2(\omega) = \pi \sum_n \frac{|F_n|^2}{2\omega_n} \delta(\omega - \omega_n) \quad (1.3)$$

In our computations, the Dirac's deltas have been substituted by normalized Gaussian distributions. In order to obtain the equivalence between (1.1), (1.2) and (1.3) we have to set F_{el} , that represents the oscillator strength of the electronic excitation, to a value that holds:

$$\epsilon_\infty = 1 + \frac{F_{el}^2}{\omega_{el}^2},$$

in which ϵ_∞ is the high-frequency dielectric constant, that has been furnished from first-principles calculations.

1.2 Raman spectrum: reduced cross-section

In a Raman scattering process, a phonon corresponding to the vibrational eigenstate ω_n is either created or destroyed.

In order to understand it better, we are going to do a brief recap of classic theory of light scattering. When invested by radiation that propagates at velocity \mathbf{v} , of frequency w and of wavelength $\lambda = \frac{2\pi v}{w}$, much greater than the system dimension, atoms and molecules display an induced dipole moment.

We consider the dipole moment $\mathbf{M} = a E_L \mathbf{e}_L$, that is induced in a material with polarization tensor a when it interacts with an electric field $\mathbf{E} = E_L \mathbf{e}_L$, polarized along \mathbf{e}_L .

As the electric field oscillates, the power emission of the oscillating dipole is given by:

$$\frac{dW_s}{d\Omega} = \frac{w^4}{(4\pi)^2 \epsilon_0 c^3} |\mathbf{e}_s \cdot \mathbf{a} \cdot \mathbf{e}_L|^2 E_L^2,$$

in which \mathbf{e}_s is the polarization of the scattered light.

When normalizing on incoming energy flux $W_L = \epsilon_0 c E_L^2$, we obtain the differential scattering cross-section

$$\frac{d\sigma}{d\Omega} = \frac{w^4}{(4\pi\epsilon_0)^2 c^4} |\mathbf{e}_s \cdot \mathbf{a} \cdot \mathbf{e}_L|^2.$$

In general, since \mathbf{a} can be anisotropic, the scattering process will lead to a change in the plane of polarization of light. Additional considerations, relative to the case of inelastic scattering with phonons, that modulates \mathbf{a} , lead to the Raman cross-section.

From now on, we focus on the non-resonant case, i.e. when the incident laser frequency is not close in energy to an electronic transition. In these conditions, a phonon of frequency ω_n can be treated as a static deformation of the system. Therefore we can define the polarizability $\alpha(\xi)$, that can be expressed as a function of normal mode coordinate ξ , from which we can get[1]:

- In the case of the Stokes Raman scattering:

$$\frac{d\sigma_s(\omega)}{d\Omega} = \frac{\omega^4}{(4\pi\epsilon_0)^2 c^4} \left| \mathbf{e}_s \cdot \frac{\partial \alpha}{\partial \xi} \cdot \mathbf{e}_L \right|^2 \frac{\hbar(n+1)}{2\omega_n} \delta(\omega - \omega_n), \quad (1.4)$$

where n is the Bose-Einstein statistics

- In the case of the anti-Stokes Raman scattering:

$$\frac{d\sigma_a(\omega)}{d\Omega} = \frac{\omega^4}{(4\pi\epsilon_0)^2 c^4} \left| \mathbf{e}_s \cdot \frac{\partial \alpha}{\partial \xi} \cdot \mathbf{e}_L \right|^2 \frac{\hbar n}{2\omega_n} \delta(\omega - \omega_n) \quad (1.5)$$

- It is convenient to define the reduced Raman cross-section:

$$\frac{d\sigma(\omega)}{d\Omega} \sim \sum_n |\mathbf{e}_s \cdot \alpha^n \cdot \mathbf{e}_L|^2 \delta(\omega - \omega_n), \quad (1.6)$$

in which α^n is the Raman tensor for the n_{th} mode, defined after the dielectric susceptibility tensor χ_{ij}

$$\alpha_{ij}^n = \sqrt{\Omega} \sum_{Ik} \frac{\partial \chi_{ij}}{\partial r_{Ik}} u_{Ik}^n. \quad (1.7)$$

From the definition of dielectric susceptibilities

$$\chi_{ij} = \frac{\partial^2 E_{tot}}{\partial E_i \partial E_j} = \frac{\partial P_i^{el}}{\partial E_j}, \quad (1.8)$$

in which E_i is the electric field along the i_{th} Cartesian direction and \mathbf{P}_{el} is the electronic polarization. We can express $\frac{\partial \chi_{ij}}{\partial r_{Ik}}$ in terms of the second order derivatives of the atomic forces with respect to the electric field[7]:

$$\frac{\partial \chi_{ij}}{\partial r_{Ik}} = \frac{\partial^2 P_i^{el}}{\partial r_{Ik} \partial E_j} = \frac{1}{\Omega} \frac{\partial^3 E_{tot}}{\partial r_{Ik} \partial E_i \partial E_j} = -\frac{1}{\Omega} \frac{\partial^2 F_{Ik}}{\partial E_i \partial E_j} \quad (1.9)$$

that permit us to apply finite electric fields and make numerical computations of the second order derivatives, as follows:

- for the diagonal terms, we consider the application of an electric field E_i , along the i_{th} Cartesian direction, of amplitude $0, \pm h, \pm 2h$, leading to the corresponding atomic forces $F(0), F(\pm h), F(\pm 2h)$:

$$\frac{d^2 F}{dE_i^2}(0) = \frac{1}{12h^2} [-F(-2h) + 16F(-h) - 30F(0) + 16F(h) - F(2h)], \quad (1.10)$$

- for the out-diagonal terms, in the hypothesis that we impose $E_i = E_j = \lambda$:

$$\frac{\partial^2 F}{\partial E_i \partial E_j} = \frac{1}{2} \frac{\partial^2 F}{\partial \lambda^2} - \frac{1}{2} \frac{\partial^2 F}{\partial E_i^2} - \frac{1}{2} \frac{\partial^2 F}{\partial E_j^2} \quad (1.11)$$

We then implemented these calculations through a C++ code in order to get the results shown in the next chapters.

Chapter 2

Application to vitreous Silica (*v-SiO₂*)

In order to verify the fairness of our implementation, we computed results for *v-SiO₂*, since its vibrational properties have been consistently studied[7].

In the first place, we obtained the vibrational density of states $G(w)$ (figure 2.1) from the frequencies ω_n , to which we acted a Gaussian broadening with $\sigma=2$ meV $\simeq 16$ cm $^{-1}$:

$$G(w) = \sum_n \delta(\omega - \omega_n) \quad (2.1)$$

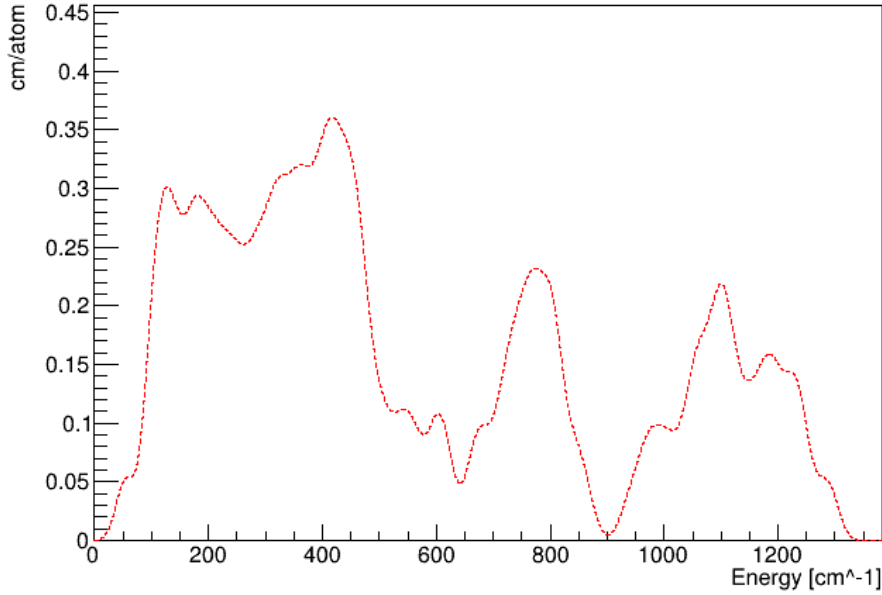


Figure 2.1: Vibrational density of states obtained through a 2 meV $\simeq 16$ cm $^{-1}$ Gaussian broadening.

Then we computed the dielectric response functions, as explained in the previous section, in which:

- the lattice constant is set at $19.4656 a_0$, where a_0 is the Bohr radius,
- the high-frequency dielectric constant is $\epsilon^\infty = 2.0$,
- the band gap is $w_{el} = 2$ eV, which permits us to set $F_{el}=2$ eV, so that $\epsilon_\infty = 1 + \frac{F_{el}^2}{\omega_{el}^2}$.

For the real part, the broadening factors η and η_{el} have been set to 0.01 eV $\simeq 80.6$ cm $^{-1}$ and, for the imaginary part, the $\delta(\omega - \omega_n)$ have been replaced by normalized Gaussian functions with $\sigma=22$ cm $^{-1}$. The two graphs are reported in figure 2.2.

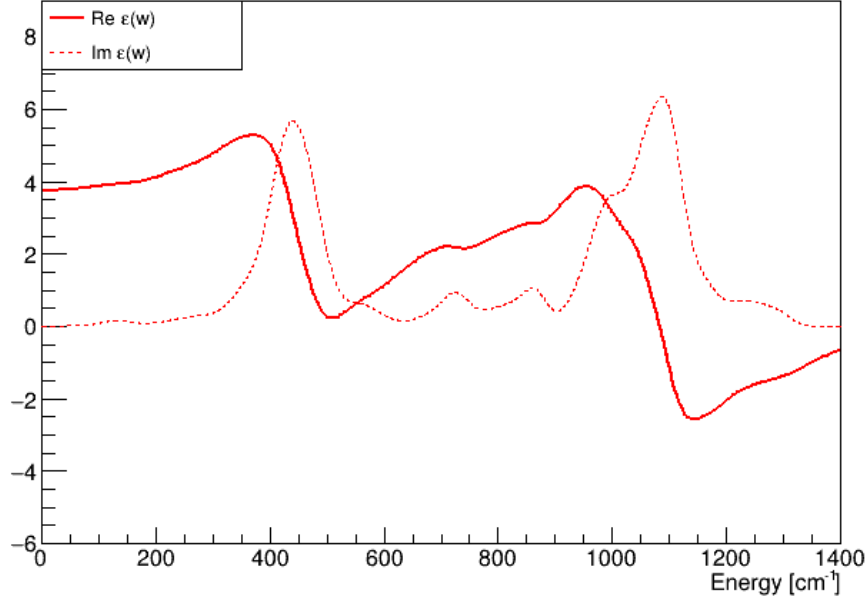


Figure 2.2: Real (solid) and imaginary (dotted) part of $v\text{-SiO}_2$ dielectric function. The broadening factors η , η_{el} of the real part have been set to $0.01\text{eV} \simeq 80.6 \text{ cm}^{-1}$, while for the imaginary part $\sigma=22 \text{ cm}^{-1}$.

Now, considering the Raman reduced cross-section, we report (figure 2.3) the graph obtained in the two following cases:

- the incoming and the outgoing photons have the same polarization: $\mathbf{e}_L = \mathbf{e}_S$, resulting in the so-called horizontal-horizontal (HH) reduced cross-section,
- the incoming and the outgoing photons have orthogonal relative polarization: $\langle \mathbf{e}_L \bullet \mathbf{e}_S \rangle = 0$, returning the horizontal-vertical (HV) reduced cross-section.

Actually, we are considering the isotropic average over crystal orientations, resulting in[3]:

$$\frac{d\sigma(\omega)_{HH}}{d\Omega} = \sum_n \left(a_n^2 + \frac{4b_n^2}{45} \right) \delta(\omega - \omega_n), \quad \frac{d\sigma(\omega)_{HV}}{d\Omega} = \sum_n \left(\frac{3b_n^2}{45} \right) \delta(\omega - \omega_n) \quad (2.2)$$

in which

$$a_n = \frac{\alpha_{11}^n + \alpha_{22}^n + \alpha_{33}^n}{3} \quad (2.3)$$

$$b_n^2 = \frac{(\alpha_{11}^n - \alpha_{22}^n)^2 + (\alpha_{11}^n - \alpha_{33}^n)^2 + (\alpha_{22}^n - \alpha_{33}^n)^2}{2} + 3[(\alpha_{12}^n)^2 + (\alpha_{13}^n)^2 + (\alpha_{23}^n)^2]$$

With the aim of making a comparison with previous studies results, we computed from $\text{Re}[\epsilon(w)]$ the static dielectric constant $\epsilon_0 = \epsilon(0) = 3.76$, in good agreement with 3.8 value reported in [7].

As far as HH and HV Raman spectra are concerned, we found optimal compatibility between the aforementioned article and our computations, for both vibrational frequencies and peaks intensities.

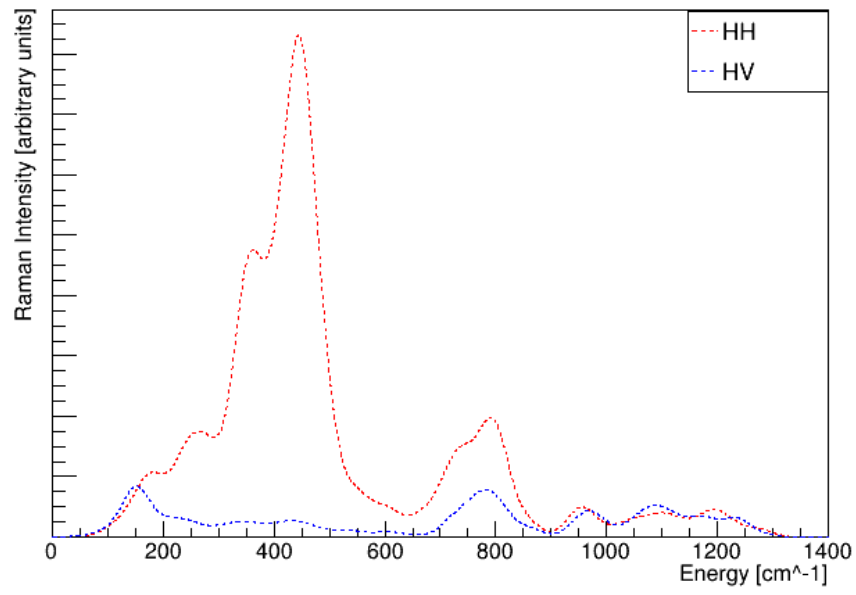


Figure 2.3: Raman reduced cross-section, broadened with normalized Gaussian distributions, $\sigma=22\text{ cm}^{-1}$.

Chapter 3

Application to methylammonium lead triiodide perovskite: $\text{CH}_3\text{NH}_3\text{PbI}_3$

We now exploit the previously exposed implementation to study the vibrational properties of hybrid organic-inorganic metal-halide perovskites, in particular $\text{CH}_3\text{NH}_3\text{PbI}_3$.

Perovskites are materials that present the crystalline structure of Calcium Titanate (CaTiO_3), that follows the general formula ABX_3 .

Representing the primitive cell in Cartesian coordinates, if we set the 'A' ion in the origin (0,0,0), 'B' is located in (0.5, 0.5, 0.5) and 'X' in (0.5, 0.5, 0), so we observe 'A' and 'B' cations coordinating respectively to 12 and 6 'X' anions, turning out in cuboctahedral and octahedral geometries.

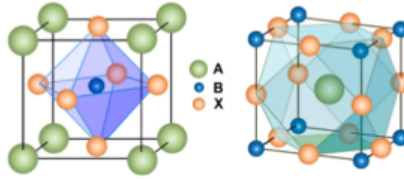


Figure 3.1: Visual representation of $\text{CH}_3\text{NH}_3\text{PbI}_3$ structure, highlighting octahedral BX_6 (on the left) and cuboctahedral AX_{12} (on the right) geometries, with $\text{A}=\text{CH}_3\text{NH}_3^+$, $\text{B}=\text{Pb}^{2+}$ and $\text{X}=\text{I}^-$.

As far as organic-inorganic metal-halide perovskites are concerned, we have that 'A' is the organic monovalent cation, in our case methylammonium (CH_3NH_3^+ , MA further on), 'B' is the divalent cation, such as Pb^{2+} and 'X' represents the halogen anion, for our structure I^- .

In particular, in our analysis, we focus on the tetragonal structure, since MAPbI_3 crystallizes in such geometry for temperatures between 162.2 and 327.4 K, that is the range of interest for photovoltaic cells activity.

Hybrid organic-inorganic perovskites have been gaining popularity since they exhibit good photovoltaic properties, both as absorber layer and as charge transport layer, thanks to their low carriers recombination rate and their relatively high mobility, resulting into diffusion length of order of magnitude of microns.

In addition, they do not require any sophisticated processing condition, the raw material is pretty affordable and it has been possible to increase their power conversion efficiency from 3.8% to 25.2% between 2009 and 2019[5], whereas it took over thirty years for other materials to obtain similar results.

The present challenge is to raise stability, lifetime and to solve toxicity issues due to lead.

In our simulation we considered a unit cell determined by a linear parameter of $16.497 a_0$, containing 48 atoms, so the equivalent of 4 times the formula $\text{CH}_3\text{NH}_3\text{PbI}_3$. Then our system will be determined by $48 \times 3 = 144$ independent orthonormal vibrational eigenmodes.

We now address the vibrational properties starting from the density of states, using formula (2.1) from

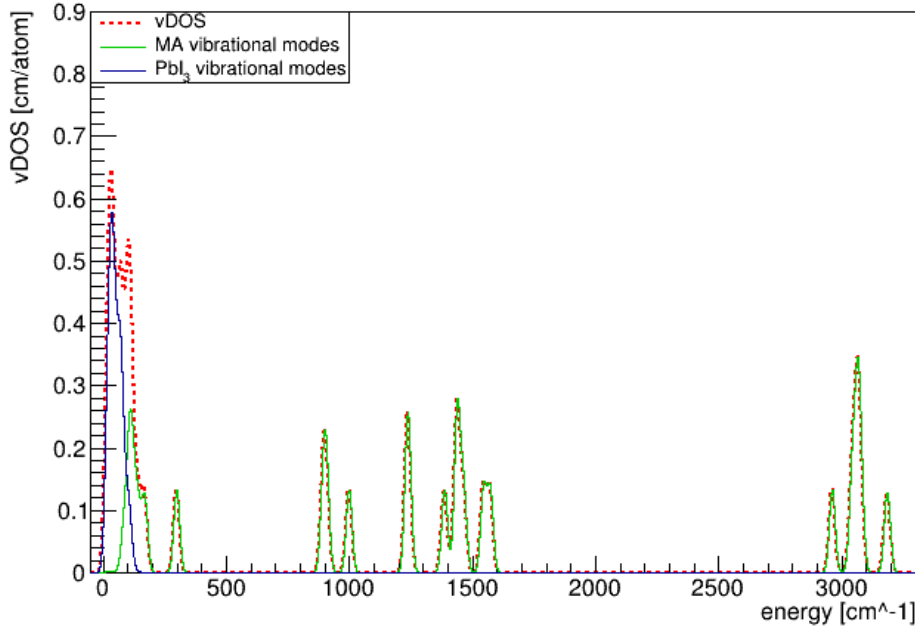


Figure 3.2: Vibrational density of states obtained through a 12 cm^{-1} Gaussian broadening: total vDOS (red solid graph), CH_3NH_3 cations contribution (dotted green), PbI_3 network contribution (blue dotted).

the previous chapter, where now we broadened our spectra through $\sigma=12 \text{ cm}^{-1}$ normalized Gaussian distributions.

In particular, we plotted the total vDOS (figure 3.2), that takes into account all the atoms in the unit cell of our simulation, then we decomposed it respectively into the MA cations and the PbI_3 network contributions, in order to highlight organic, inorganic and mixed modes.

The vibrational spectrum extends up to 3200 cm^{-1} , displaying pure MA cations modes between 250 and 3200 cm^{-1} , that correspond to internal vibrations of organic ions, resulting in:

- a spectral line around 300 cm^{-1}

and two main groups of peaks:

- $880\text{-}1600 \text{ cm}^{-1}$, showing six relative maxima around 901, 999, 1238, 1387, 1440 and 1568 cm^{-1}
- $3015\text{-}3210 \text{ cm}^{-1}$, showing three relative maxima around 2962, 3064 and 3185 cm^{-1} .

Furthermore, as reported in [3], the density of states of a single CH_3NH_3^+ molecule belonging to the organic structure resembles the vibrational spectrum of the isolated MA cation, meaning that the inter-cation coupling, despite giving rise to collective modes, is small.

On the other hand, in the low-frequency range, $0\text{-}200 \text{ cm}^{-1}$, organic and inorganic contributions are both present: the total vDOS displays a main peak around 34 cm^{-1} , due to PbI_3 internal modes, since, as highlighted in [3], the contributions of the rotations of the inorganic octahedra network are negligible. Further, the 105 cm^{-1} maximum shows off from MA spinning around the C-N axis, whereas 71 cm^{-1} peak is due to mixed organic-inorganic modes.

Through our algorithm, we were then able to plot the real (1.2) and imaginary (1.3) part of the infrared dielectric function, in which we focused our attention on energy transitions between $0\text{-}35 \text{ meV}$, equivalent to $0\text{-}282 \text{ cm}^{-1}$.

Theoretical parameters, returned by previous DFPT computations, and broadening factors η , η_{el} , σ have been set to the following values:

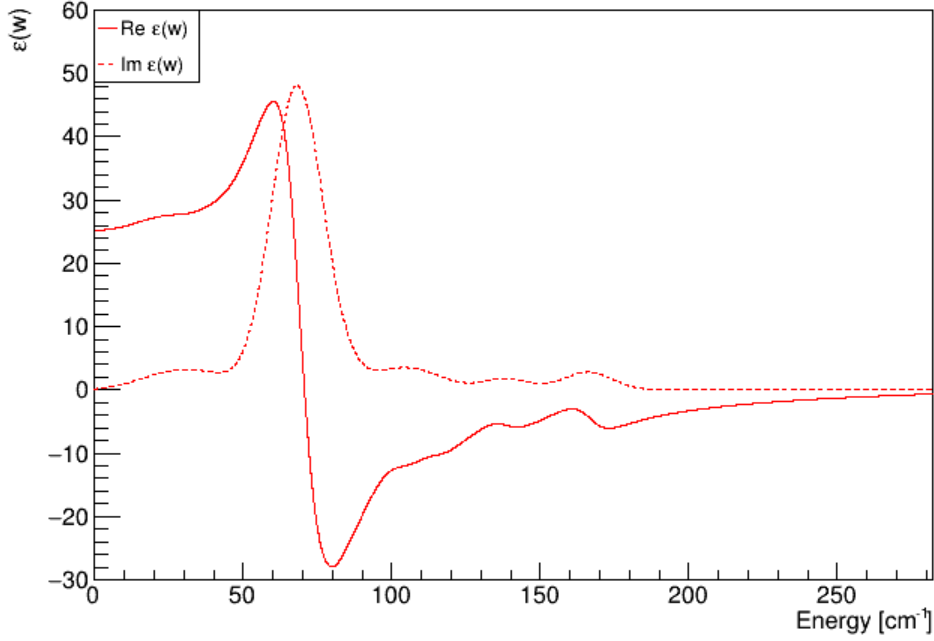


Figure 3.3: Real (solid) and imaginary (dotted) part of the MAPbI₃ dielectric function. The broadening factors η , η_{el} for the real part have been set to 16 cm⁻¹, while for imaginary part $\sigma=8$ cm⁻¹.

ϵ^∞	5.6
w_{el}	1.55
F_{el}	6.64
η	16 cm ⁻¹
η_{el}	16 cm ⁻¹
σ	8 cm ⁻¹

In particular, we obtain the static dielectric constant $\epsilon_0=25.5$, in good agreement with previous results [9], that set it to 25.7.

As far as the Raman spectrum is concerned, we computed the reduced cross-section through (2.2), at first considering the HH and HV reduced cross-sections along the full vibrational range: 0-3200 cm⁻¹ (figure 3.4). We obtained, as expected, that horizontal-horizontal polarization intensity is higher than horizontal-vertical one, in particular, of about a factor 2 in the whole frequencies range.

Three main peaks regions are shown, as it could have been inferred from vDOS:

- considering low frequencies, 15-310 cm⁻¹ range, with the main peak around 65 cm⁻¹,
- 880-1600 cm⁻¹ region, displaying 5 relative maxima, the brighter one being around 1550 cm⁻¹,
- the range between 1940-3210 cm⁻¹ energies, where the full spectrum absolute maximum is found, at about 3068 cm⁻¹.

In order to match the Raman peaks with the correspondent vibrational modes, we decomposed the reduced cross-section intensity in the MA organic cations and the PbI₃ network contributions, by selecting or ignoring the corresponding $\{I\}$ components in atomic displacements $u_{I,j}^n$.

We do here a brief recap of vibrations.

Stretching mode is the changing in the bond length. Bending motions include all the vibrational modes in which the angle between two bonds changes. One of them is rocking, that happens when the change concerns the angle between a group of atoms and the rest of the molecule.

Translations, libration and spinings are rigid-body motions, that means that the relative positions of the involved atoms do not change. Librations happen when the compound undergo small oscillations

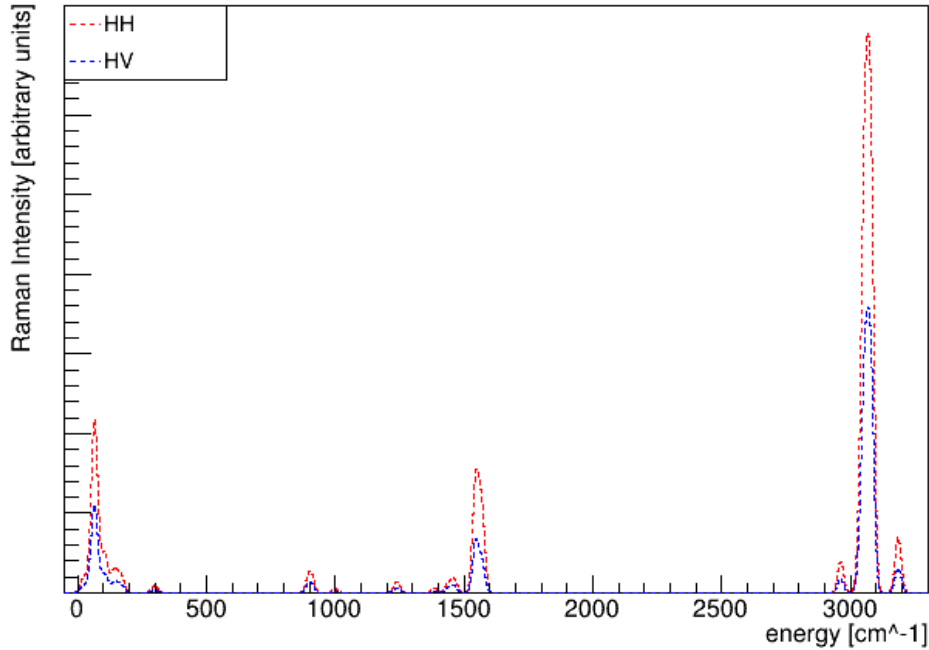


Figure 3.4: Raman reduced cross-section, broadened with normalized Gaussian distributions, $\sigma=12 \text{ cm}^{-1}$.

around the equilibrium orientation. Spinning corresponds to the rotation of two groups of the molecule around an axis.

For clarity's sake, henceforth we focus on the HH light polarization.

As far as the entire spectrum is concerned (figure 3.5), we can observe that Raman peaks in $300\text{--}3200 \text{ cm}^{-1}$ region, the main being centered at 300, 895, 999, 1241, 1387, 1460, 1545, 1569, 2961, 3055, 3186 cm^{-1} are exclusively attributable to organic cations activities, and in particular to their internal vibrations, corresponding to N-H, C-H and C-N stretching modes, CH_3NH_3 rocking modes and CH_3NH_3 torsional modes.[3]

After that, we zoomed into the low-frequency range (figure 3.6): $0\text{--}200 \text{ cm}^{-1}$, where organic rigid-body motions and inorganic vibrational modes are both contributing.

From now on, to obtain our spectra, we used a Gaussian smearing of 2 cm^{-1} , in order to match the precision of the experimental results we will exploit hereafter.

Giving a closer look, we can observe that the two cross-section components show little overlap, resulting in almost no mixed modes, from which it can be inferred that organic-inorganic substructures inter-coupling is negligible. Therefore, from now on, we can proceed having distinct vibrational analysis of MA cations and PbI_3 network.

The lowest frequencies range, between $0\text{--}85 \text{ cm}^{-1}$ is determined by inorganic cage modes: the 20 cm^{-1} feature stems from Pb-I-Pb rocking motions, the 31, 35, 62, 65 and 72 cm^{-1} peaks are attributed to Pb-I-Pb bending modes, in which the last three represent the most intense lines in the $0\text{--}200 \text{ cm}^{-1}$ range. Moving to higher frequencies, we encounter the 101, 104 and 113 cm^{-1} peaks, assigned to Pb-I stretching but mainly to librations and translations of MA cations, whereas the 138, 145 cm^{-1} frequencies arise from organic structures spinning around C-N axis.

Finally, at 167 and 173 cm^{-1} we find MA cations librations and translations.

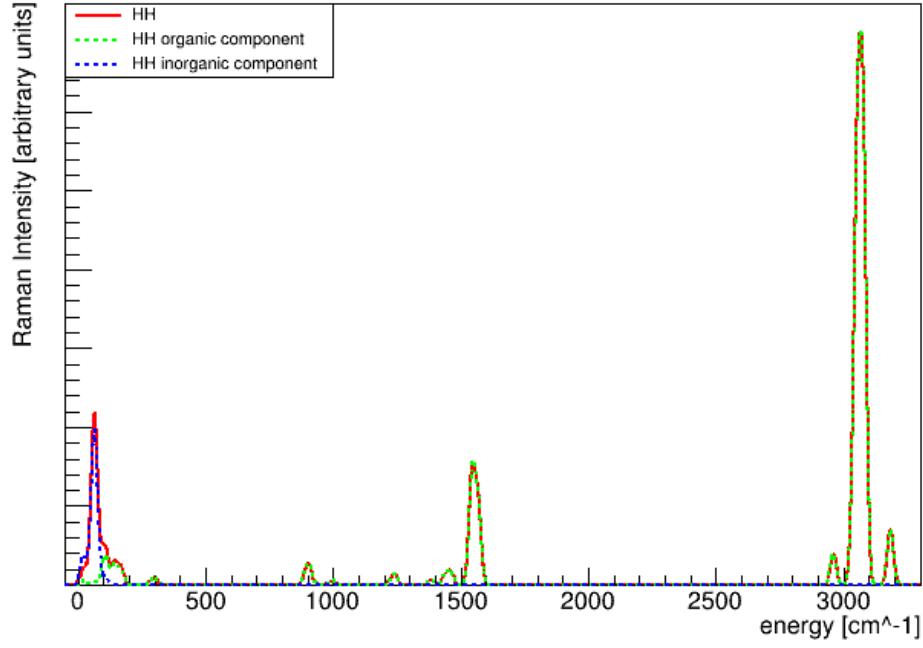


Figure 3.5: Raman HH reduced cross-section, considering the whole simulation cell (red line), the MA organic cations (green dotted) and the inorganic PbI_3 network (blue dotted) contributions in the $0\text{--}3200\text{ cm}^{-1}$ range. A Gaussian broadening with $\sigma=12\text{ cm}^{-1}$ has been exploited for all of the three curves.

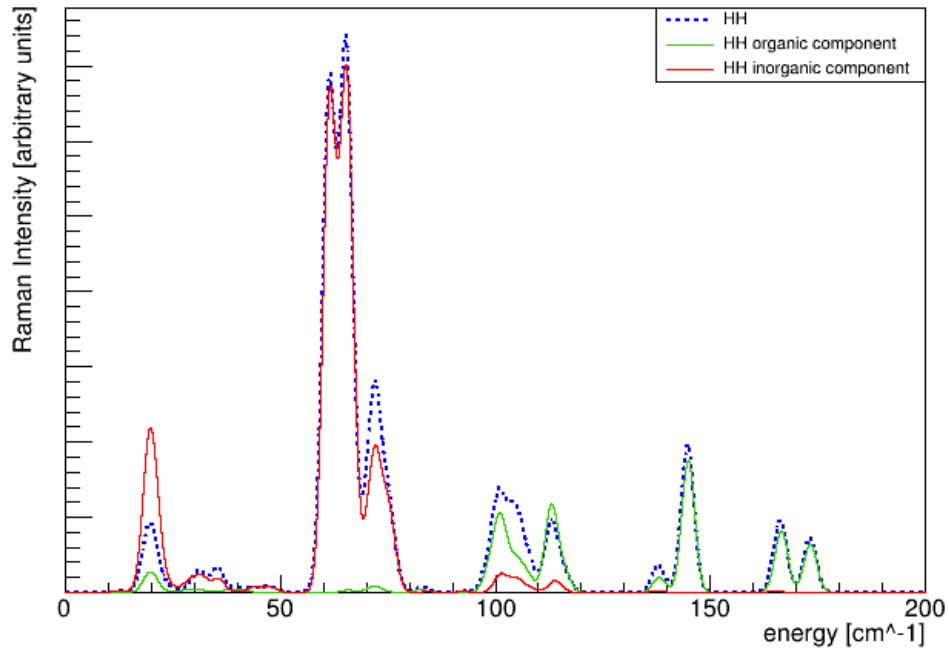


Figure 3.6: Raman HH reduced cross-section, considering the whole simulation cell (red line), the MA organic cations (green dotted) and the inorganic PbI_3 network (blue dotted) contributions in the $0\text{--}200\text{ cm}^{-1}$ range. A Gaussian broadening with $\sigma=2\text{ cm}^{-1}$ has been exploited for all of the three curves.

3.1 Comparison of measured and computed Raman spectra

From the previous analysis of the first-principles computed Raman spectrum in the low-frequency range, we can now get the comparison with the measured Raman spectrum.

In particular, we exploit the experimental results presented in [3], that have been acquired for single crystals of orthorhombic MAPbI₃ held at 4 K. Whereas in our simulation we considered tetragonal phase perovskite, it is more convenient, as far as measured Raman is concerned, to consider the low temperature orthorhombic configuration, otherwise degradation would lead to the presence of PbI₂ in the sample, that would add spurious peaks around 94 and 110 cm⁻¹.

This phase difference has to be taken into account when comparing the two spectra: since orthorhombic and tetragonal phases are mainly distinguished by MA cations orientations, they could give rise to distinct librational modes intensities.[4]

Overall, we found good agreement between the computed and measured frequencies and relative intensities for most of the peaks: this allows us to propose the same assignment of [3] for the vibrational nature of the measured peaks.

For frequencies smaller than 50 cm⁻¹, we observe PbI₃ internal modes: 9 cm⁻¹ line is assigned to Pb-I-Pb rocking modes, whereas 26, 32, 42 and 49 cm⁻¹ peaks arise from Pb-I-Pb bending modes.

Further on, the 85, 97 features are both due to Pb-I stretching modes, but the first one actually is the superposition of inorganic internal motions and MA cations librations and translations. Finally, the 58, 142 cm⁻¹ peaks stem from vibrational modes corresponding to rigid-body motions of the organic structures. We resume in table 3.1 the computed frequencies of the main vibrational modes and their nature, and in table 3.2 the experimental results[3], that are also shown in figure 3.7.

Comparing the two, we notice two main differences:

- experimental peaks appear to be red-shifted of about 10-25 cm⁻¹: this could be due to the fact that in our first-principles calculations we neglected Van der Waals (VdW) interactions, spin-orbit coupling (SOC) and anharmonicity. These factors lead to small corrections to vibrational eigenmodes, Born effective-charge tensors and dielectric constants[3]. On the other hand, anharmonicity can play an important role in MA cations rigid-body vibrational modes and VdW interactions and SOC can blueshift or redshift peaks of about 15 cm⁻¹.
- the 142 cm⁻¹ measured peak turned out to have noticeably smaller intensity with respect to the correspondent computed modes: this has been found out also from previous studies[3] but, even if several hypotheses have been formulated, the effective cause is still unclear. In our case also the fact that we are comparing orthorhombic and tetragonal phases can play a role[4].

frequency [cm ⁻¹]	vibrational modes
20	Pb-I-Pb rocking
31	Pb-I-Pb bending
35	Pb-I-Pb bending
62	Pb-I-Pb bending
65	Pb-I-Pb bending
72	Pb-I-Pb bending
101	Pb-I stretching and libration/translation
104	Pb-I stretching and libration/translation
113	Pb-I stretching and libration/translation
138	spinning
145	spinning
167	libration/translations
173	libration/translations

Table 3.1: Computed Raman peaks and corresponding vibrational modes.

frequency [cm^{-1}]	vibrational modes
9	Pb-I-Pb rocking
26	Pb-I-Pb bending
32	Pb-I-Pb bending
42	Pb-I-Pb bending
49	Pb-I-Pb bending
58	libration/translation
85	Pb-I stretching and libration/translation
97	Pb-I stretching
142	libration/translation

Table 3.2: Experimental Raman peaks[3] and corresponding vibrational modes.

3.2 Inorganic network contribution

We are particularly interested in the inorganic contributions to the Raman spectrum, since, through having a deeper understanding of it, we could infer vibrational results for other hybrid organic-inorganic perovskites, obtained by substituting I^- with another halogen anion, as Cl^- , Br^- , F^- or Pb^{2+} with a different divalent cation among Sn^{2+} , Ge^{2+} or 2 atoms of monovalent alkali cation as Li^+ , Na^+ , K^+ , Rb^+ , Cs^+ [5]. This could lead to achieve the aim of resolving the lead-related toxicity issue.

In order to foresee the vibrational properties of others metal-halide perovskites, we concentrate on the inorganic Raman cross-section, considering separately Pb^{2+} and I^- contributions.

From the graph of figure 3.8, we can observe that the low-frequency peak displayed in PbI_3 network spectrum around 20 cm^{-1} , that derives from Pb-I-Pb rocking mode, is almost completely due to lead contribution. In fact, in Pb partial spectrum, a peak of similar intensity and with the same centroid is found. We could then expect a change in this feature when substituting lead with another XIV group element: in particular, as reported in [5], considering Br^- , that has a smaller ionic radius than I^- , result in stiffer bonds, that lead to a reduced lattice constant and to a more stable phase. Further on, it has been observed[4] that increasing the compound order, e.g. decreasing temperature, or through the aforementioned atoms switch, results into a frequency "blue shift" and intensity decrease in the correspondent Raman peak.

Since ionic radius shrinks along a group, going from MAPbI_3 to MASnI_3 to MAGeI_3 , we would expect to find the peak that corresponds to the considered stretching mode translated at higher frequencies and with smaller intensity. On the other hand, we foresee a negligible difference when changing the halide since iodine doesn't contribute to this feature.

The 62, 65 and 72 cm^{-1} peaks result to turn out from both lead and iodine concurrence, in a 1:4 contribution. We would then expect some differences in the spectrum, following the above mentioned qualitative argument, both when changing halogen anions or XIV group divalent cations or either of the two atom types.

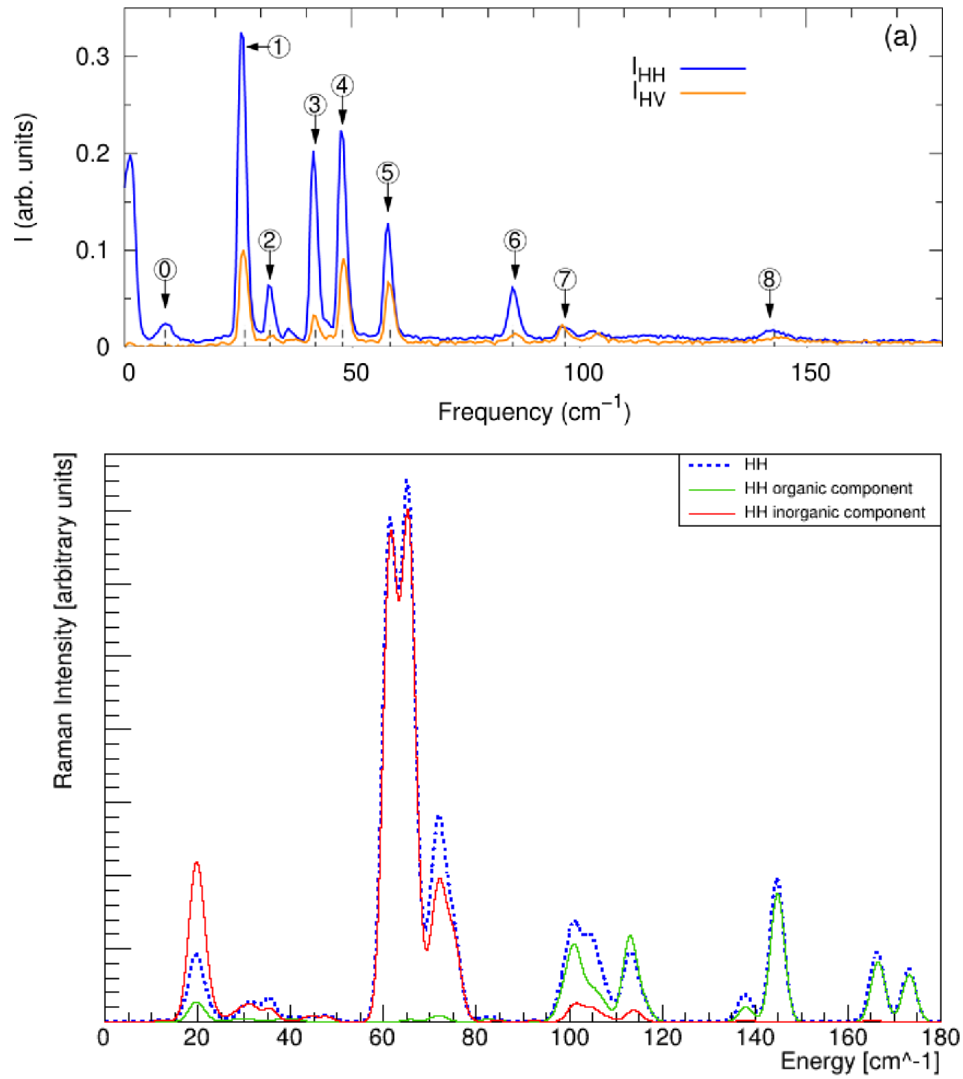


Figure 3.7: Comparison between computed and measured Raman spectra.

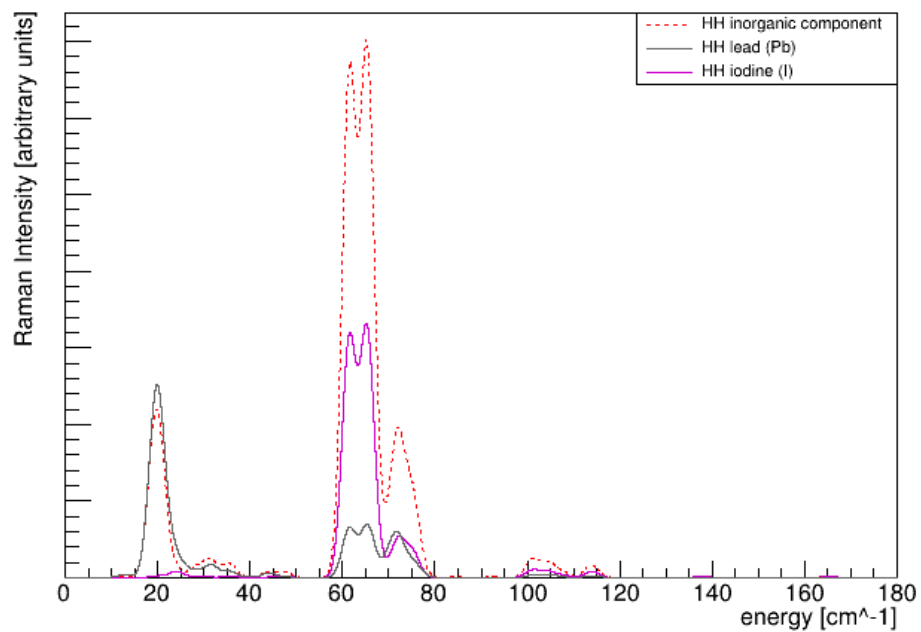


Figure 3.8: Raman reduced cross-section, broadened with normalized Gaussian distributions, $\sigma=2$ cm⁻¹.

Conclusion

The aim of this thesis work has been the analysis of the vibrational properties of the methylammonium lead triiodide perovskite.

In order to achieve this target, we implemented a C++ algorithm to calculate the vibrational density of states, the infrared dielectric function and the Raman reduced cross-section.

At first, we verified the fairness of our implementation by computing the aforementioned quantities for vitreous silica, getting a good agreement with previous studies results[7].

Then, we calculated the same spectra for the methylammonium lead triiodide perovskite: MAPbI₃. Its vibrational density of states extends up to 3200 cm⁻¹ and presents three main regions: the low-frequency range at about 0-300 cm⁻¹, the middle one between 880-1600 cm⁻¹ and the higher one around 3015-3200 cm⁻¹.

From the real part of the dielectric function, we computed ϵ_0 , that turned out to be 25.5, in good agreement with previous studies[9], that set its value at 25.7.

From the Raman spectrum analysis, we could identify the vibrational modes of the main peaks.

In particular, we could point out the following three main regions. At the lowest frequencies, between 0-72 cm⁻¹, PbI₃ network internal modes, such as Pb-I-Pb rocking and bending are found. The 101-173 cm⁻¹ range stems out from MA cations rigid-body motions, including librations, translations and spinning around C-N axis. Also Pb-I stretching contributions are present. In the end, from 300 to 3200 cm⁻¹ we assigned the observed features to internal vibrations of the organic structure.

Thanks to the good agreement with the experimental results[3], we could match the 0-142 cm⁻¹ range measured peaks to the corresponding vibrational modes. We have pointed out that the inorganic cage motions cause the 9-85 cm⁻¹ peaks and methylammonium internal modes give rise to the 58-142 cm⁻¹ region.

The observed frequency-shift between measured and calculated spectra can be due to fact that in our computations we neglected van der Waals interactions, spin-orbit coupling and anharmonicity.

Finally, we exploited our algorithm to analyze the inorganic network contribution to the Raman spectrum, to foresee the vibrational behaviour of other methylammonium metal-trihalide perovskites.

Bibliography

- [1] M. Cardona et al. *Light Scattering in Solids II: Basic Concepts and Instrumentation*. Topics in Applied Physics. Springer Berlin Heidelberg, 1982.
- [2] Arti Mishra et al. “One-dimensional Facile Growth of MAPbI₃ Perovskite Micro-rods”. In: *RSC Advances* 9 (Apr. 2019).
- [3] Miguel A. Pérez-Osorio et al. “Raman Spectrum of the Organic–Inorganic Halide Perovskite CH₃NH₃PbI₃ from First Principles and High-Resolution Low-Temperature Raman Measurements”. In: *The Journal of Physical Chemistry C* 122.38 (2018), pp. 21703–21717.
- [4] Claudio Quarti et al. “The Raman Spectrum of the CH₃NH₃PbI₃ Hybrid Perovskite: Interplay of Theory and Experiment”. In: *The Journal of Physical Chemistry Letters* 5.2 (2014), pp. 279–284.
- [5] Priyanka Roy et al. “A review on perovskite solar cells: Evolution of architecture, fabrication techniques, commercialization issues and status”. In: *Solar Energy* 198 (2020), pp. 665–688.
- [6] W. J. Tipping et al. “Stimulated Raman scattering microscopy: an emerging tool for drug discovery”. In: *Chem. Soc. Rev.* 45 (8 2016), pp. 2075–2089.
- [7] P. Umari and Alfredo Pasquarello. “Infrared and Raman spectra of disordered materials from first principles”. In: *Diamond and Related Materials* 14 (Aug. 2005), pp. 1255–1261.
- [8] Paolo Umari, Edoardo Mosconi, and Filippo De Angelis. “Infrared Dielectric Screening Determines the Low Exciton Binding Energy of Metal-Halide Perovskites”. In: *The Journal of Physical Chemistry Letters* 9.3 (2018), pp. 620–627.
- [9] Zhuo Yang et al. “Unraveling the Exciton Binding Energy and the Dielectric Constant in Single-Crystal Methylammonium Lead Triiodide Perovskite”. In: *The Journal of Physical Chemistry Letters* 8.8 (2017), pp. 1851–1855.